Journal of Materials Chemistry A

ROYAL SOCIETY OF CHEMISTRY

REVIEW

Cite this: *J. Mater. Chem. A*, 2020, **8**, 10695

Carbon-based single-atom catalysts for CO_2 electroreduction: progress and optimization strategies

Xiu-Li Lu, Xin Rong, Chao Zhang* and Tong-Bu Lu *

Received 19th February 2020
Accepted 30th April 2020

DOI: 10.1039/d0ta01955k

rsc.li/materials-a

The electrochemical CO_2 reduction reaction (CO_2 RR) is a promising route to convert CO_2 into industrial chemicals and fuels. The viability of CO_2 electroreduction depends critically on developing highly active and selective electrocatalysts. As a new frontier in the field of catalysis, carbon-based single-atom catalysts (SACs) with atomically dispersed metal catalytic sites have shown great potential for CO_2 electroreduction, and offer opportunities for an in-depth understanding and clear identification of the active sites at the atomic level. In addition, the tunable local environment of metal atoms and supports in SACs made it possible to optimize their electrocatalytic performances for CO_2 reduction. However, controllable synthesis and optimization of carbon-based SACs for high-efficiency CO_2 RR remain rather challenging. Herein, we summarize the recent advances in the synthesis of carbon-based SACs for CO_2 RR, and discuss the mechanisms as well as the influencing factors during the catalytic process. Moreover, some optimization strategies for carbon-based SACs towards CO_2 electroreduction are highlighted. At the end of this review article, we present an outlook on the challenges and prospects in this specific research area.

1. Introduction

Ever since the advent of the industrial revolution, the consumption of fossil fuels has been continuously increasing, leading to the excessive emission of carbon dioxide (CO_2) greenhouse gas,[1–3] and the resulting severe consequences of climate change and environmental crisis have caused great trepidations in the scientific community and the public.[4–6] It is thus of urgent necessity to develop CO_2 mitigation technologies so as to deal with these challenges.[7,8] Among the most scrutinized technologies, the electrochemical CO_2 reduction reaction (CO_2 RR) stands out as a promising chemical fixation strategy for the conversion of CO_2, which can serve as a cost-effective and clean C1 resource for manufacturing value-added chemicals and fuels. When integrated with sustainable and clean energy sources (such as solar or wind energy), the

MOE International Joint Laboratory of Materials Microstructure, Institute for New Energy Materials and Low Carbon Technologies, School of Materials Science & Engineering, Tianjin University of Technology, Tianjin 300384, China. E-mail: colin_august@sina.com; lutongbu@tjut.edu.cn

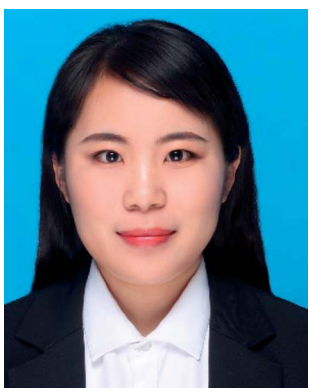

Xiu-Li Lu is an associate professor in the Institute for New Energy Materials and Low Carbon Technologies, School of Materials Science and Engineering, Tianjin University of Technology. She received her PhD degree in 2016 from the University of Science and Technology of China. Her research focuses on developing carbon-based materials for photo/electro-catalytic reactions, including water splitting reaction and carbon dioxide conversion.

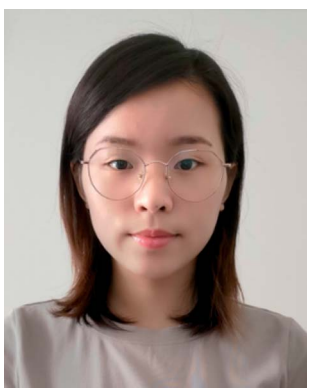

Xin Rong obtained her B.S. from the College of Chemistry and Chemical Engineering, Liaocheng University in 2017. Currently she is a PhD student at the Institute for New Energy Materials and Low Carbon Technologies, School of Materials Science and Engineering, Tianjin University of Technology, supervised by Professor Tong-Bu Lu. Her current research revolves around single-atom catalysts for CO_2 electroreduction, with the intention of achieving high faradaic efficiency at high current density.

electrochemical CO_2 RR can effectively store these intermittent renewable energies in stable compounds and help balance the power grid.[9–12] Besides, the electrochemical CO_2 RR can be conducted under relatively mild and readily controllable conditions. Thus, the study of the electrochemical CO_2 RR has become a research hotspot.[13,14] However, the electrochemical CO_2 RR is a complicated process typically with rather sluggish kinetics. The reduction process strongly depends on cathode catalysts and the conditions of electrolysis, and may involve two-, four-, six-, eight- or twelve-electron pathways for the generation of products including CO, HCOOH, HCHO, CH_3OH, CH_4, C_2H_4, respectively.[15] For a breakthrough in electrochemical CO_2 RR, it is crucial to regulate and enhance the selectivity for a specific reduction product during the catalytic process and meanwhile to suppress the competing reaction of hydrogen evolution.[16]

The development of highly active and selective electrocatalysts for CO_2 reduction is still underway. Recently, carbon-based single-atom catalysts (SACs) fabricated with atomically dispersed metal ions on various supports have garnered broad interest as a promising class of electrocatalysts for CO_2 RR. In this review, we will focus on the latest progress in carbon-based SACs for electrochemical CO_2 RR, and put emphasis on optimization strategies for boosting the catalytic performances of electrochemical CO_2 RR. At the end of this paper, we will discuss the challenges and prospects faced by carbon-based SACs for CO_2 electroreduction.

2. SACs for CO_2 electroreduction

During the past few decades, a variety of electrocatalysts, such as metals,[17–19] alloys,[20] metal oxides,[21–23] metal sulphides[24,25] and metal phosphides,[26,27] have been developed as potential candidates for CO_2 electroreduction. The reduction products are closely related to the catalytic materials and their structures. For examples, metallic Sn[28] and Bi[29] show the ability to convert CO_2 mainly into formate or formic acid, whereas CO is the primary product over Au[17] and Ag.[30] However, the unsatisfactory activity and selectivity of these catalysts impede their practical applications. As is well known, downsizing catalyst particles usually leads to optimization of their electronic structures and exposure of more active sites.[31–33] When the size of metal particles is reduced to isolated single atoms, the so-called SACs can be obtained. As a new class of advanced materials, SACs generally feature maximized metal utilization and active metal centers with low coordination numbers and adjustable structures, as well as high activity and tunable selectivity for catalytic reactions.[34] Since the first report by Qiao *et al.*,[35] SACs have been widely studied as promising electrocatalysts for hydrogen evolution reaction (HER),[36] oxygen reduction reaction (ORR)[37] and CO_2 RR.[38,39] The unique advantages of SACs qualify them as efficient electrocatalysts for CO_2 RR with high selectivity, providing the ideal models for understanding the relationship between the structures of SACs and their catalytic performances.[40,41] Notably, carbon-based SACs show great potential for CO_2 electroreduction. For example, Pan *et al.* prepared a Co SAC with the $Co–N_5$ coordination environment dispersed on N-doped porous carbon supports, which shows excellent performances for CO_2 RR, with nearly 100% CO selectivity and a remarkable stability.[42] This $Co–N_5$ active site was proved capable of promoting the rapid formation of the important COOH* intermediate and the desorption of the CO product. Gu *et al.* reported an Fe SAC that could produce CO at an overpotential of 80 mV and deliver a current density of 94 mA cm^{-2} at an overpotential of 340 mV.[43] The results of *in situ* X-ray absorption spectroscopy and electrochemical tests showed that the Fe^{3+} atoms coordinated to pyrrolic nitrogen atoms function as the active sites, which enable easier CO_2 adsorption and CO

Chao Zhang is working as a professor at the Institute for New Energy Materials and Low Carbon Technologies, School of Materials Science and Engineering, Tianjin University of Technology. He received his PhD degree in 2011 from Peking University. Then he worked as a research assistant in the Department of Physics, the Chinese University of Hong Kong, and as a postdoctoral research fellow in the College of Chemistry and Molecular Engineering, Peking University. His early research interest was focused on rare earth and noble metal functional materials; currently his interest is in developing high-efficiency catalytic materials for electrochemical energy conversion and storage.

Tong-Bu Lu obtained his B.S. in 1988 and PhD in 1993 from Lanzhou University. After a two years postdoctoral fellowship at Sun Yat-Sen University, he joined the faculty at the same University, and became a professor in 2000. He worked as a postdoctoral researcher in F. Albert Cotton's group at Texas A&M University in 1998 and 2002. He moved to Tianjing University of Technology in 2016. His current research interest is artificial photosynthesis catalysts, including water splitting and CO_2 reduction catalysts. He has over 260 scientific publications. He was supported by the National Natural Science Foundation for Distinguished Youth Scholar in 2006. Now, he is a fellow of Royal Society of Chemistry (FRSC), and is a member of the Editorial Advisory Board of CrystEngComm.

desorption than conventional Fe^{2+} sites. Besides carbon supports, metal oxides and metals have also been reported as supports to fabricate SACs for CO_2 electroreduction.[38] For example, Wang *et al.* reported a Cu-doped CeO_2 SAC with rich oxygen vacancies for electrocatalytic CO_2-to-CH_4 conversion with a faradaic efficiency of 58%.[38a] To date, great effort has been devoted to developing high-efficiency SACs with a variety of metal sites for CO_2 RR, and scientists have made rapid advances. Considering that most of the SACs developed thus far for CO_2 electroreduction are based on carbon-related supports, and that optimization of the synthesis process and design of more active metal sites in carbon-based C-SACs are still the hot topics in this area, in this review we would focus on carbon-based SACs, and discuss the related advances.

2.1 Synthesis of SACs

Owing to the high surface energy of isolated metal atoms, the synthesis of stable and high-efficiency SACs is generally rather challenging. Up to now, great advances have been made in designing C-SACs for electrochemical CO_2 RR by various strategies, such as ZIF-assisted synthesis[43–47] ion adsorption strategy,[48] high-temperature migration[49,50] and multistep pyrolysis.[51,53,54]

The ZIF-assisted synthesis strategy is an important method for preparing SACs, such as Co,[45] Ni,[46] Fe[43] and Cu[47] SACs. For example, a Cu SAC has been synthesized by anchoring isolated Cu sites on through-hole carbon nanofibers (CuSAs/TCNF), with Cu/ZIF-8 nanoparticles as the Cu source.[47] As shown in Fig. 1a, firstly, a mixed solution of Cu/ZIF-8 and polymer was electrospun into nanofibers, which were annealed and then etched with acids. The resulting CuSAs/TCNF could be directly used as the electrode for CO_2 RR, with a high faradaic efficiency (FE) of 44% for methanol, and a high partial current density of 93 mA cm^{-2} for C1 products. In addition, Bi *et al.* fabricated graphene-based Ni SACs (Ni^{2+}@NG) by a facile ion adsorption strategy.[48] As shown in Fig. 1b, isolated Ni(II) cyclam-like moieties were formed *via* ion adsorption and mild annealing. The resulting

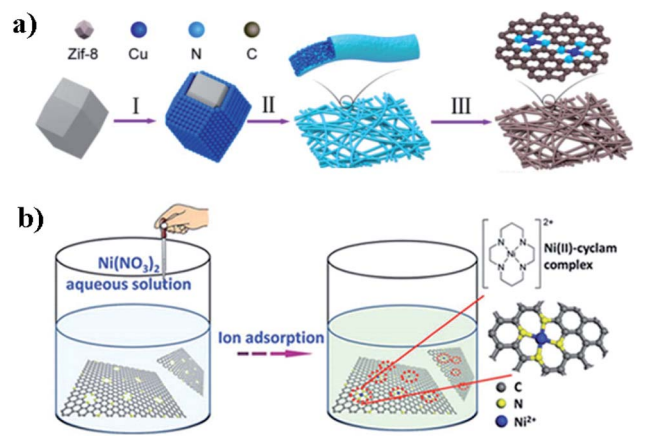

Fig. 1 Schematic illustration of the fabrication of CuSAs/TCNF (a)[47] and Ni^{2+}@NG (b).[48] Copyright 2019, American Chemical Society (a) and Copyright 2018, Wiley-VCH (b).

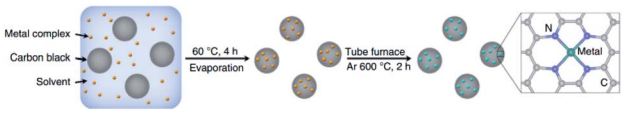

Fig. 2 Schematic illustration of the preparation of Ni-NCB.[55] Copyright 2019, Nature Publishing Group.

Ni^{2+}@NG showed a high FE of 92% for CO with a current density of 10.2 mA cm^{-2} at −0.86 V.

Scaling up the preparation of SACs in cost-effective ways is critical for their practical applications. Large-scale synthesis of SACs has been realized on the basis of commercial carbon black.[55,56] For instance, Yang *et al.* reported a versatile route to prepare various SACs by adsorbing metal–phenanthroline complexes onto commercial carbon black and subsequent pyrolysis under an Ar atmosphere (Fig. 2).[55] This method could produce SACs with high metal loadings in large quantities (>1 kg). A Ni SAC (Ni-NCB) thus prepared showed a high activity for CO_2 RR with a high FE of 98.9% at −1.2 V.

Controlled synthesis of SACs with defined coordination environments of metal sites is crucial for optimizing the activity and selectivity. It has been found that the coordination environment of metal sites in SACs is greatly influenced by the parameters during the synthesis of SACs, including the choice of metal and carbon sources, and the pyrolysis temperature. For example, researchers have tuned the coordination number of Co sites in Co-based SACs by controlling the volatile C–N fragments through changing the pyrolysis temperature.[45] As a result, three Co SACs could be prepared with Co–N_4, Co–N_3 and Co–N_2 coordination sites at 800, 900 and 1000 °C, respectively. The more unoccupied 3d orbitals in Co–N_2 can strengthen the adsorption of the $CO_2^{\bullet-}$ intermediate, and thus the Co–N_2 SAC shows the highest activity for CO_2 RR, with a FE of 94% for CO and a current density of 18.1 mA cm^{-2} at an overpotential of 520 mV. Recently, we have synthesized a vacancy-defect Ni SAC (Ni–N_3–V) using $NiCl_2 \cdot 6H_2O$, cyanuric acid (CA) and 2,4-diamino-6-phenyl-1,3,5-triazine (DPT) as the precursors.[51] As shown in Fig. 3, the oxygen and nitrogen atoms in CA and DPT can simultaneously coordinate to Ni to form a N/O mixing coordinated Ni–N_3O SAC, in which the coordinated O atom can be selectively removed at 800 °C owing to the weaker Ni–O coordination bond, resulting in a vacancy-defect Ni–N_3–V SAC at the Ni site. In contrast, the reaction of $NiCl_2 \cdot 6H_2O$ with the precursor simply containing nitrogen atoms (DPT) can only generate a non-vacancy-defect Ni–N_4 SAC. In addition, at about 460 °C, during the synthesis of Ni–N_3–V and Ni–N_4 SACs, the precursors would undergo a melting process and turn into

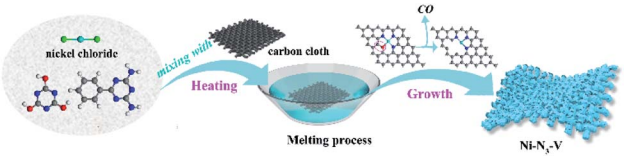

Fig. 3 Schematic illustration of the synthesis of Ni–N_3–V grown on carbon cloth.[51] Copyright 2019, Wiley-VCH.

a liquid mixture, which could be coated on carbon cloth or other substrates, generating a binder-free electrode with N–N_3–V and Ni–N_4 SACs grown on. The results of experiments and DFT calculations reveal that the presence of a vacancy-defect in Ni–N_3–V can dramatically boost the catalytic activity for the CO_2-to-CO conversion, with a large current density of 65 mA cm^{-2} and a FE over 90% at −0.9 V *vs.* RHE, as well as a record high turnover frequency of 1.35×10^5 h^{-1}.

2.2 Characterization techniques for SACs

The detailed structural information of SACs, such as the atomic structure and distribution of metal atoms, the amount of metal loading and the surface properties, is of vital importance for the development of SACs and their application in CO_2 electroreduction. In this section, we will mainly introduce two characterization techniques for the structures of SACs, electron microscopy and X-ray absorption spectroscopy (XAS).

Scanning electron microscopy (SEM) and transmission electron microscopy (TEM) can identify the overall morphologies and structures of samples. For SACs, the measurements of SACs under a spherical aberration corrected transmission electron microscope, especially in the STEM mode, are powerful means to determine their atomic structures and elemental compositions. In particular, the high-angle annular dark field (HAADF) image obtained with atomic resolution could unveil the dispersion of isolated metal atoms anchored on the carbon supports, because of the large difference of atomic numbers between metal and carbon atoms. For example, the bright spots in Fig. 4b and c correspond to the nickel atom sites, which are separately dispersed on carbon nanotubes.[49] In addition, electron energy loss spectroscopy (EELS) and mapping measurements could be used to analyze the structural information of surface elements and their distribution.

As an important characterization technique, XAS has been widely used to probe the structures and the local chemical environments of metal atoms in SACs. As for the applications of XAS in electrocatalysis, we refer interested readers to a review article recently published by Wang *et al.*[52] XAS data typically include the pre-edge, X-ray near-edge absorption structure (XANES) and extended X-ray absorption fine structure (EXAFS). XANES could reflect the electronic structures of metal atoms, such as the oxidation states and unoccupied electronic states. EXAFS can reveal the information regarding the coordination number, the bond distance, bond types, *etc.* For example, as shown in Fig. 4d and e, the N and C K-edge spectra for F-CPs are similar to those of H-CPs (Ni SAC, obtained by acid-leaching F-CPs), demonstrating the stability of nitrogen doped carbon supports during the acid-leaching process. In addition, as shown in Fig. 4e, the energy of the pre-edge in the XANES spectrum for H-CPs is higher than that of Ni foil and lower than that of NiO, indicating that the valence state of Ni atoms in H-CPs is $Ni^{\delta+}$ ($0 < \delta < 2$). In addition, as shown in Fig. 4g, the intensity of the Ni–Ni bond in H-CPs is notably decreased compared with that of F-CPs, and a new peak assigned to Ni–N coordination is observed, indicating that the majority of Ni NPs could be removed after an acid leaching process.[49] The fitting results from the FT-EXAFS can provide the coordination numbers of metal atoms in SACs.[51,54] For example, as shown in Fig. 5, the topo-chemical transformation of Ni–N_4–C from Ni-doped g-C_3N_4 was verified by the EXAFS.[53] The local chemical configurations for Ni-doped g-C_3N_4 and Ni–N_4–C were determined by the FT curves of Ni K-edge EXAFS. As demonstrated in Fig. 5b and c, no notable peaks for Ni–Ni bonds were observed, showing that the Ni atoms in Ni-doped g-C_3N_4 and Ni–N_4–C are dispersed as isolated atom sites. The quantitative simulation of

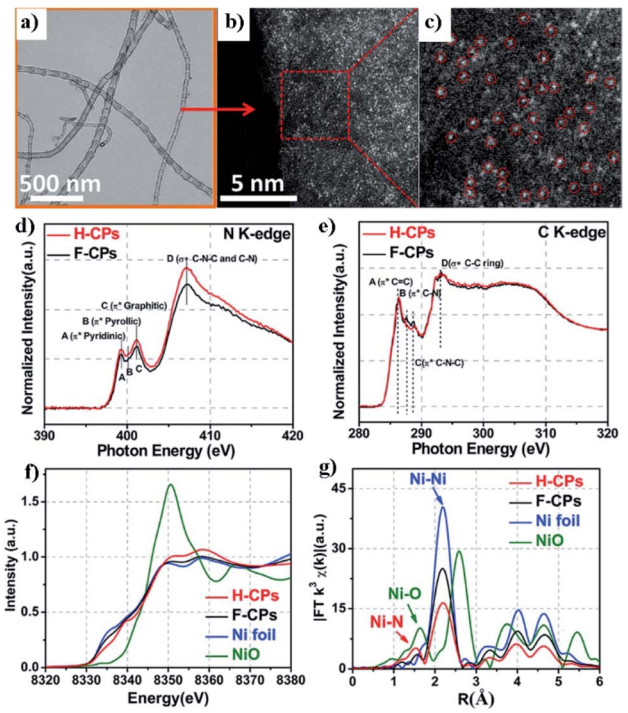

Fig. 4 (a–c) The TEM (a) and HAADF (b and c) images for H-CPs. (d and e) The N K-edge (d) and C K-edge (e) XAS spectra of H-CPs and F-CPs. (f and g) The Ni K-edge XANES spectra (f) and Fourier transform (FT) of Ni K-edge EXAFS spectra (g) of comparison samples.[49] Copyright 2019, Cell Press.

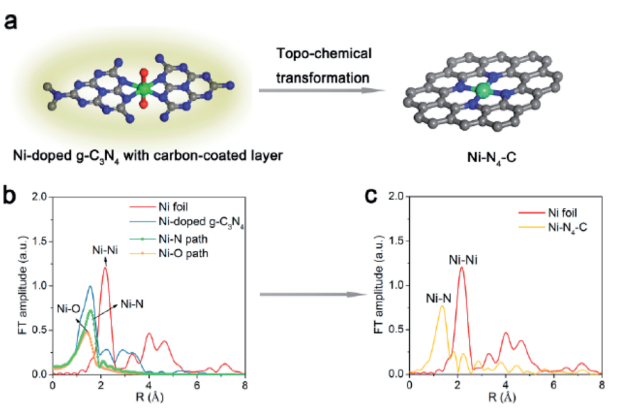

Fig. 5 (a) Schematic illustration of the topo-chemical transformation of Ni–N_4–C from Ni-doped g-C_3N_4. (b, c) The Ni K-edge XANES spectra of Ni-doped g-C_3N_4 (b) and Ni–N_4–C (c).[53] Copyright 2017, American Chemical Society.

Table 1 Structural parameters obtained from the EXAFS fitting

	Pair	N	R (Å)	σ^2 ($\times 10^{-3}$ Å^2)	E_0 (eV)
Ni-doped g-C_3N_4	Ni–O	2.0	1.95 ± 0.02	11.0 ± 1.2	−8.0
	Ni–N	4.0	2.09 ± 0.02	6.2 ± 0.6	−6.0
Ni–N_4–C	Ni–N	4.0 ± 0.5	1.86 ± 0.02	7.3 ± 0.7	−0.6

EXAFS reveals that the Ni atom in g-C_3N_4 is coordinated by four N atoms (1.95 Å) and two O atoms (2.09 Å), whereas the Ni atom in the obtained Ni SAC is coordinated by four N atoms (1.86 Å). The fitting parameters are shown in Table 1.

2.3 Electrocatalytic performance of SACs for CO_2 RR

The isolated metal atoms in SACs act as the active sites for CO_2 reduction. To get a brief overview of the performances of SACs for CO_2 RR, we summarized some representative SACs, categorized by the metal atoms in Table 2. Obviously, the performance of SACs for CO_2 RR is strongly dependent on the metal sites, supports and the preparation conditions (such as reaction temperature, time and preparation methodology). In addition, it can be seen from Table 2 that a high metal loading does not necessarily guarantee a high current density, probably because for SACs with high metal loadings, a considerable number of metal atoms are encapsulated within the carbon materials, with low accessibility for reactant molecules. Therefore, the catalytic activities of SACs are predominantly related to those metal atoms anchored on the accessible surface. Besides, the high surface energy of separately dispersed metal atoms also imposes a great challenge on the stability of SACs.

In this section, we will discuss the influence of the interface species surrounding the single atoms on the catalytic properties of SACs. Zhang *et al.* reported a FeN_5 SAC, which showed a high FE of CO at a low overpotential of −0.35 V, much higher than that of the FeN_4 SAC.[67] Compared with the traditional FeN_4 structure, FeN_5 features an additional axial ligand with a pyrrolic nitrogen, which provides the p_x and p_y orbitals to form p–d coupling with the Fe atom, and thus lowers the electron density of the Fe 3d orbitals, resulting in the weak interaction between CO and Fe sites and the rapid desorption of CO.

Table 2 Representative SACs with different metal atoms for electrocatalytic CO_2RR

SACs	Name	CE	Electrolyte	CO_2 reduction products [FE%]	Current density (mA cm^{-2})	Metal contents (wt%)	Stability (h)	Ref.
Fe	Fe^{3+}–N–C	Fe–N_4 (pyrrolic-N)	0.5 M $KHCO_3$	CO >90% (H-cell)	21 (at −0.47 V *vs.* RHE)(H-cell)	2.80	12 (at −0.37 V *vs.* RHE)	43
				CO >90 (flow cell)	99 (at −0.45 V *vs.* RHE) (flow cell)			
	Fe–N–C	Fe–N_4 (pyridinic-N)	0.1 M $KHCO_3$	CO ∼87.0%	18.0 (at −0.90 V *vs.* RHE)	2.14	_	57
	Fe/NG-750	Fe–N_4 (pyridinic-N)	0.1 M $KHCO_3$	CO ∼80.0%	7.20 (at −0.80 V *vs.* RHE)	0.52	10 (at −0.60 V *vs.* RHE)	58
	Fe–N–C	Fe–N_4	0.1 M $KHCO_3$	CO ∼93.0%	16.0 (at −0.90 V *vs.* RHE)	0.46	20 (at −0.58 V *vs.* RHE)	59
Co	Co–N_5/HNPCSs	Co–N_5 (pyrrolic-N)	0.2 M $NaHCO_3$	CO ∼99.4%	17.5 (at −0.90 V *vs.* RHE)	3.54	10 (at −0.73 V *vs.* RHE)	42
	Co_1–N_4	Co–N_4	0.1 M $KHCO_3$	CO ∼82.0%	23.4 (at −1.00 V *vs.* RHE)	0.60	10 (at −0.80 V *vs.* RHE)	60
	Co–N_2	Co–N_2	0.5 M $KHCO_3$	CO ∼95.0%	45.0 (at −0.90 V *vs.* RHE)	0.25	60 (at −0.63 V *vs.* RHE)	45
Ni	Ni^{2+}@NG	Ni–N_4 (pyridinic-N)	0.5 M $KHCO_3$	CO ∼92%	30.0 (at −0.88 V *vs.* RHE)	0.80	20 (at −0.58 V *vs.* RHE)	48
	Ni–N–C	Ni–N_4 (pyridinic-N)	0.1 M $KHCO_3$	CO ∼96%	22.0 (at −0.96 V *vs.* RHE)	2.83	9 (at −0.75 V *vs.* RHE)	57
	NiSA–N–CNTs	Ni–N_4	0.5 M $KHCO_3$	CO ∼91.3%	25.5 (at −0.70 V *vs.* RHE)	20.0	12 (at −0.55 V *vs.* RHE)	54
	Ni–N_4–C	Ni–N_4 (pyridinic-N)	0.5 M $KHCO_3$	CO ∼99%	28.6 (at −0.81 V *vs.* RHE)	1.41	30 (at −0.81 V *vs.* RHE)	53
	Ni-SAC	Ni–N_4	0.1 M $KHCO_3$	CO ∼98.9%	13.5 (at −1.60 V *vs.* RHE)	2.50	20 (at −0.80 V *vs.* RHE)	55
	A-Ni-NG	Ni–N_4	0.5 M $KHCO_3$	CO ∼97%	88.0 (at −1.00 V *vs.* RHE)(RDE)	4.60	_	61
	Ni SAs/N–C	Ni–N_3C	0.5 M $KHCO_3$	CO ∼71.9%	10.48 (at −1.00 V *vs.* RHE)	1.53	60 (at −1.0 V *vs.* RHE)	46
	Ni–N_3–V	Ni–N_3–V (pyridinic-N)	0.5 M $KHCO_3$	CO ∼94%	65.0 (at −0.90 V *vs.* RHE)	2.30	14 (at −0.70 V *vs.* RHE)	51
	C–Zn_1–Ni_4 ZIF-8	Ni–N_2–V_2	0.5 M $KHCO_3$	CO ∼98%	77.0 (at −1.03 V *vs.* RHE)	5.44	12 (at −0.63 V *vs.* RHE)	62
	H-CPs	Ni–N_x	0.5 M $KHCO_3$	CO ∼97%	48.66 (at −1.00 V *vs.* RHE)	_	40 (at −1.0 V *vs.* RHE)	49
	Ni–N-Gr	Ni–N_x	0.1 M $KHCO_3$	CO ∼95%	4.00 (at −1.20 V *vs.* RHE)	2.20	5 (at −0.65 V *vs.* RHE)	63
Cu	CuSAs/TCNFs	Cu–N_4	0.1 M $KHCO_3$	CH_3OH ∼44% CO ∼56%	85.0 (at −1.10 V *vs.* RHE)	1.30	50 (at −0.90 V *vs.* RHE)	47
Zn	ZnNx/C	Zn–N_4	0.5 M $KHCO_3$	CO ∼95%	18.0 (at −0.90 V *vs.* RHE)	0.10	75 (at −0.43 V *vs.* RHE)	64
Bi	Bi SAs/NC	Bi–N_4	0.1 M $NaHCO_3$	CO ∼97%	23.0 (at −0.90 V *vs.* RHE)	0.20	4 (at −0.50 V *vs.* RHE)	65
Sn	AD-Sn/N–C1000	Sn–N_x (pyridinic-N)	0.1 M $KHCO_3$	CO ∼91%	17.5 (at −1.00 V *vs.* RHE)	1.0	24 (at −0.60 V *vs.* RHE)	66

As shown in Fig. 6a, the desorption energy of CO on FeN_4 sites is very large, higher than the free energy for the further protonation, indicating that the CO molecule would be trapped on the FeN_4 sites and thus leading to the poor selectivity for CO production. Recently, Gu *et al.* reported an Fe^{3+}–N–C SAC with Fe atoms coordinated to pyrrolic N ligands, and investigated its performance for CO_2 electroreduction to CO.[43] The electrochemical data and operando XAS characterization results showed that the pyrrolic N ligands could stabilize the Fe atoms with the +3 oxidation state, which are more active for CO_2 electroreduction with faster CO_2 adsorption and weaker CO adsorption, compared with Fe atoms coordinated to pyridinic N ligands (as in Fe^{2+}–N–C).

Besides the coordination environment of metal atoms in SACs, the defects surrounding the metal-N species could also greatly affect the performances of SACs. For example, Yan *et al.* reported a Ni SAC with coordination-unsaturated Ni–N sites, which could reach a high CO current density of 71.5 mA cm^{-2} at −1.03 V *vs.* RHE and a high CO FE of 92.0% to 98.0% over −0.53 to −1.03 V *vs.* RHE.[62] As shown in Fig. 6b, four types of Ni–N structures (including NiN_4, NiN_3, NiN_3V and NiN_2V_2) have been used as models to calculate the free energy diagrams for CO_2RR and HER on Ni sites. As depicted in Fig. 6c, the free energy of *COOH (G^*_{COOH}) on NiN_4 is the highest, and the desorption of *CO is the most difficult for NiN_3 among the four types of SACs, demonstrating the high activity of coordination-unsaturated Ni sites in NiN_3V and NiN_2V_2 for CO_2 RR. In addition, NiN_2V_2 exhibits the highest selectivity for CO_2-to-CO conversion with a lower G_{*COOH} (0.62 eV) than G_{*H} (0.69 eV).

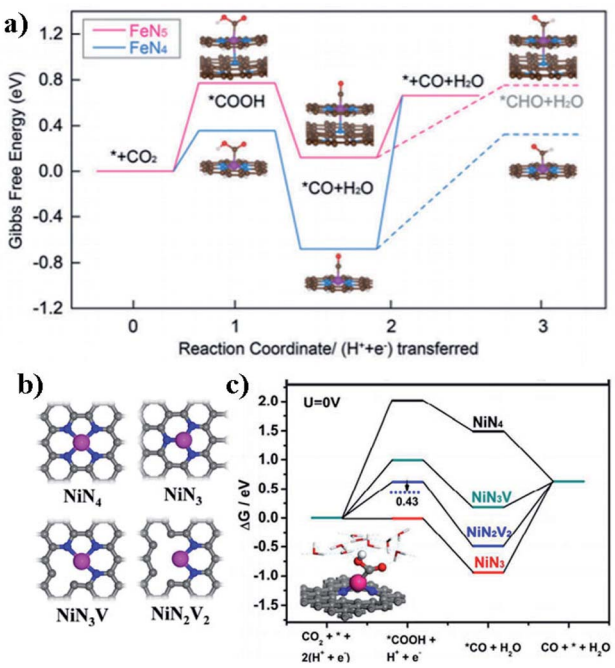

Fig. 6 (a) Free energy profiles with the optimized intermediates during the electrocatalytic CO_2 to CO reaction.[67] Copyright 2019, Wiley-VCH. (b and c) Four types of proposed Ni–N structures (b) and the corresponding free energy diagrams for CO_2 RR (c). Ref. 62 Copyright 2018, Elsevier.

Because electrochemical CO_2 RR requires three-phase (solid–liquid–gas) contact, optimizing the surface properties and the microstructure of the supports in SACs is also an effective way to improve the adsorption of CO_2 and elevate the CO_2 RR performance. For example, Yang *et al.* constructed a CuSAs/TCNTs catalyst with isolated Cu atoms decorated through-hole carbon nanofibers, which showed CO_2 RR performances superior to those of CuSAs/CNTs with the atomic Cu decorated carbon nanofibers.[47] The through-hole structure of CuSAs/TCNTs led to an extremely high CO_2 adsorption capacity, which is about 20 times higher than that of CuSAs/CNTs. And the electrochemical active surface area (ECSA) of CuSAs/TCNTs is 23.3 mF cm^{-2}, three times higher than that of CuSAs/CNTs (7.2 mF cm^{-2}). As shown in Fig. 7, both the through-hole structure and isolate Cu sites are responsible for the partial current density of C1 products for CuSAs/TCNTs in comparison with CuSAs/CNTs and TCNTs.

In addition, the stability of SACs has also been an issue of intense scrutiny. It has been suggested that the coordination between metal atoms and the heteroatoms in the carbon support significantly contribute to the formation of stable SACs, and the heteroatoms can influence the stability of SACs. For instance, Yang *et al.* found that Ni NPs supported on N-rich carbon could yield Ni SACs after calcination, whereas Ni NPs on N-free carbon would further aggregate (Fig. 8a and b).[50] Theoretical calculations revealed that the Ni atoms have a high affinity to pyridinic and pyrrolic N atoms, which explains the atomic dispersion after calcination. Gu *et al.* prepared two Fe SACs with different coordinating N atoms, namely Fe^{3+}–N–C (with pyrrolic N) and Fe^{2+}–N–C (with pyridinic N).[43] They employed *in situ* XAS to probe the stability of SACs under different potentials. As shown in Fig. 8c and d, Fe^{3+}–N–C undergoes the conversion from Fe^{3+} to Fe^{2+} at 0.5 V *vs.* RHE, and Fe^{2+}–N–C undergoes the same process at −0.2∼−0.1 V *vs.* RHE. These results indicate that pyrrolic N atoms can better stabilize the Fe^{3+} species during the electrocatalysis. Therefore, the stability of SACs can be improved by tuning the coordinating heteroatoms.

Recent studies have also demonstrated that the stability of SACs can also be improved by judicious design of self-supported electrodes. For example, Yang *et al.* reported a flexible and self-supported single-atom Ni-decorated porous carbon membrane

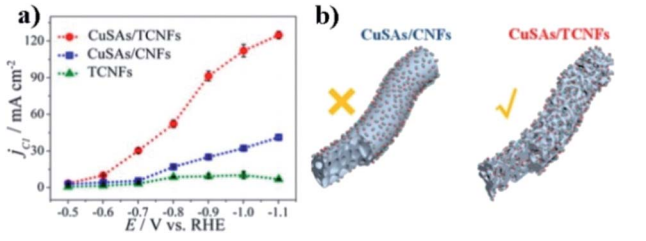

Fig. 7 (a) Partial current densities for C1 products of CuSAs/TCNFs (isolated Cu atoms anchored on through-hole carbon nanofibers), CuSAs/CNFs (isolated Cu atoms anchored on carbon nanofibers) and TCNFs (through-hole carbon nanofibers). (b) Schematic illustration of CO_2 diffusion on CuSAs/CNFs and CuSAs/TCNFs. Ref. 47 Copyright 2019, American Chemical Society.

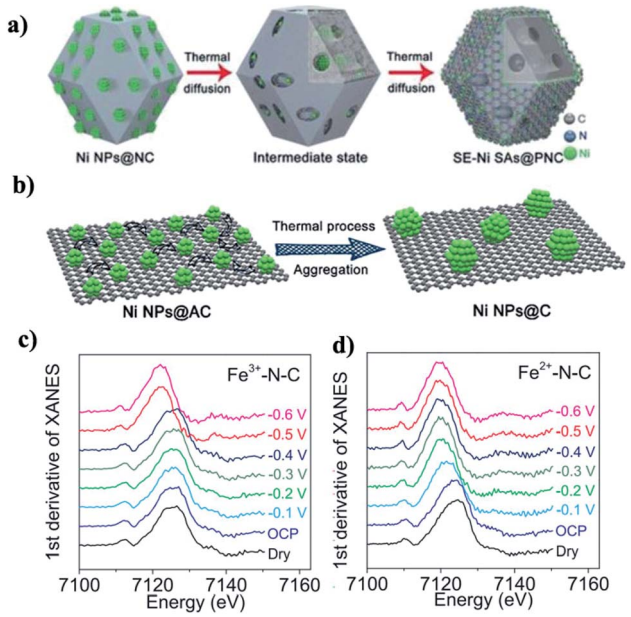

Fig. 8 (a and b) The transformation of Ni NPs into Ni single atoms on N-doped carbon (NC) supports (a) and on the non-defective XC-72 carbon (AC) supports (b). Copyright 2018, Wiley-VCH. Ref. 50. (c and d) Operando XAS characterization for Fe^{3+}–N–C and Fe^{2+}–N–C in the CO_2-saturated 0.5 M $KHCO_3$ catholyte. Copyright 2019, Science, Ref 43.

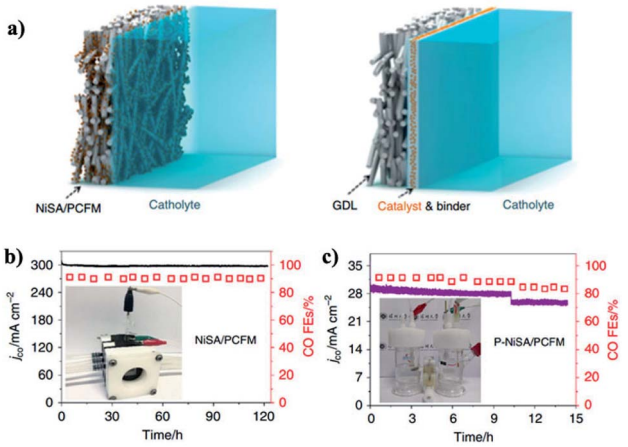

Fig. 9 (a) NiSA/PCFM membrane directly used as the GDE and a typical GDE cell with catalyst powder loaded onto a gas-diffusion layer *via* the polymer binder. (b and c) Long-term stability tests in the GDE cell (b) and f H-type cell (c) at −1.0 V RHE, respectively. Copyright 2020, Nature Publishing Group. Ref 68.

(NiSA/PCFM membrane) for CO_2 electroreduction.[68] As shown in Fig. 9a, this membrane can be directly used as a gas diffusion electrode (GDE), with no additional adhesive layers, forming a stable three-phase interface for the catalysis. As a result, the stability of this electrode in GDE devices is far superior to that in conventional H-type electrolyzers (Fig. 9b and c). This work demonstrates that the design of electrodes is also of importance for optimizing the activity and stability of SACs applied in CO_2 electroreduction.

2.4 Mechanism studies

The electrocatalytic CO_2 RR mainly involves the following elementary steps: (1) the adsorption of CO_2 on the active sites; (2) the formation of intermediates from the adsorbed CO_2 molecule; (3) the formation of the reduction product; (4) the desorption of the reduction product.[69,70] To understand the reaction mechanism, some *in situ* characterization technologies, such as *in situ* XAS, *in situ* Raman and *in situ* IR spectra, have been widely used to monitor the change of metal ion valence states, as well as the *in situ* formed intermediates during the electrocatalytic CO_2 reduction process.[71–74]

For example, Liu *et al.* fabricated a Ni SAC (denoted as Ni-CNT-CC) with a well-defined Ni–N_4 structure (Fig. 10a), and found that the Ni^+ ions resulting from the *in situ* Ni^{2+} reduction are the real active sites. The rate-determining step of CO_2 RR is $*CO_2^- + H^+ \rightarrow *COOH$.[74] As shown in Fig. 10b, c, the *in situ* X-ray absorption spectra were recorded to investigate the change of Ni sites during the CO_2 RR process. With a cathodic bias, the rising edge in Ni-K edge XANES was shifted to lower energy with ~0.3 eV in Ar-saturated $KHCO_3$, indicating the conversion from Ni^{2+} to Ni^+ (Fig. 10b). After CO_2 was bubbled into Ar-saturated $KHCO_3$, the Ni^+ at 0.2 V *vs.* RHE was converted back to Ni^{2+}. Moreover, in CO_2-saturated $KHCO_3$, the rising edge in Ni-K edge XANES remained unchanged under cathodic potential (Fig. 10c). In combination with further measurements of near-ambient- pressure X-ray photoelectron spectroscopy, electrochemical characterization and *in situ* Raman spectra, it was verified that the Ni sites in Ni-CNT-CC undergo the reduction from Ni^{2+} to Ni^+ under cathodic bias, and the Ni^+ sites could be quickly oxidized back to Ni^{2+} by CO_2. In addition, the electrochemical kinetics was further investigated by comparing the reaction orders of CO_2 and H^+, to identify the rate-determining

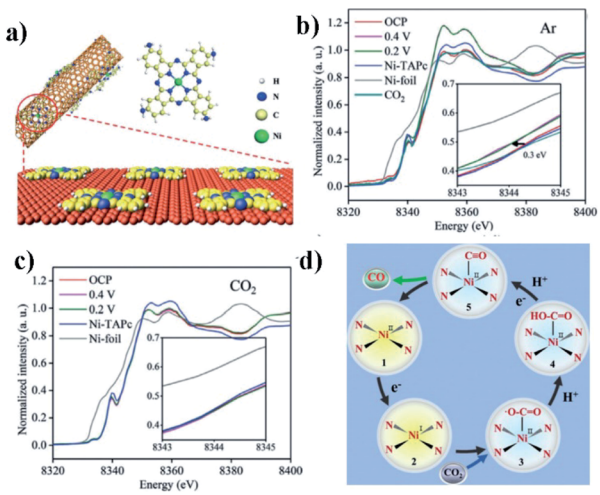

Fig. 10 (a) The synthesis of Ni-CNT-CC with a well-defined Ni–N_4 structure. (b and c) *In situ* XAS measurements. Normalized Ni K-edge XANES spectra obtained at various applied potentials (*vs.* RHE) in 0.5 M $KHCO_3$ under Ar (b) and CO_2 atmospheres (c); inset, enlarged Ni K-edge XANES. (d) The proposed CO_2RR pathway for Ni-CNT-CC.[74] Copyright 2019, Wiley-VCH.

step. The proposed CO_2 RR pathway is shown in Fig. 10d, and the rate-determining step is the one from "3" to "4".

Besides the *in situ* characterization technologies, theoretical calculations have also been usually used in combination with experimental results to understand the catalytic mechanism and the relationship between the structure of metal species and the catalytic performances. For example, Ju *et al.* studied the nature of carbon-based SACs with M–N_4 sites (M: Mn, Co, Fe, Ni and Cu) at the atomic level by investigating their potential-dependent CO and H_2 selectivity during CO_2 RR (Fig. 11a and b).[75] As shown in Fig. 11c and d, three regions with distinct reaction kinetics were identified during electrocatalysis. Region 1 (around −0.45 V *vs.* RHE) was related to the first proton-coupled electron transfer process ($CO_2 + H^+ + e^- \rightarrow COOH^*$). The experimental results show that Cu, Fe, and Mn need a small overpotential, whereas Cu and Ni need a larger one with the weakest binding to COOH*. At region 2 (around −0.6 V *vs.* RHE), the CO TOF is linearly related to the binding energy of CO*, which comes from the process: $COOH^* + H^+ + e^- \rightarrow CO^* + H_2O$. This showed that the rate-controlling intermediate has been changed from COOH* to CO*; at region 3 (large overpotential regime, <−0.7 V *vs.* RHE), the CO faradaic efficiencies of Ni and Cu SACs (Fig. 11b) were still growing along with applied potentials because of the small CO* binding energy (region 2) and weak H* binding (from the completing hydrogen evolution reaction, $H^+ + e^- \rightarrow H^* \rightarrow H_2$). In contrast, the CO faradaic efficiencies for Fe, Co and Mn SACs (Fig. 11b) have passed their maxima because of their downhill reaction energy pathways for the hydrogen evolution reaction. The reason for the much lower experimental TOF of Cu SACs than that of Ni SACs is that the Cu ions were unstable and could be reduced to metallic Cu nanoparticles. This work systematically studied the performances of the series of SACs for CO_2 RR with an in-depth understanding of their mechanisms.

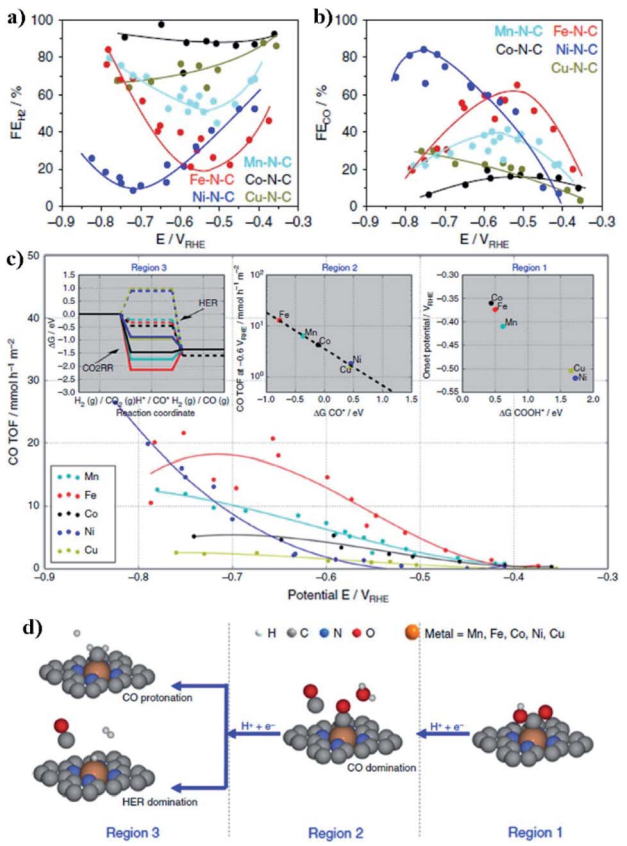

Fig. 11 (a) The H_2 and (b) CO FE of SACs with M–N_4 sites. (c) The turnover frequency of CO for SACs with M–N_4 sites. The inset is the calculated results of catalytic trends for different potential ranges, including region 1 (low potential range), region 2 (middle potential range) and region 3 (high potential range). (d) The reaction pathways correspond to the three regions in the inset of (c). Copyright 2017, Nature Publishing Group, ref 75.

Recently, the free-energy pathway and corresponding free energies for CO_2 reduction to CO on Ni SACs with different coordination environments have been investigated.[51] As shown in Fig. 12, the energies of *COOH formation and CO* desorption significantly depend on the coordination environments of Ni SACs. Notably, the presence of a vacancy-defect at the Ni site in Ni–N_3–V plays a key role in optimizing the energy barriers for the formation of *COOH and the desorption of CO*, resulting in the highest electrocatalytic activity for CO_2 electroreduction.

Notably, the intermediates during CO_2 RR primarily determine the final products. For example, Zu *et al.* employed *in situ* Fourier transform infrared spectroscopy and Gibbs free energy calculations, and confirmed that Sn SACs with $Sn^{\delta+}$ on N-doped graphene could stabilize the $*CO_2^{\bullet-}$ and $*HCOO^-$ intermediates. Therefore, the catalyst showed a high FE for formic acid rather than CO.[76]

Obviously, the catalytic performance of SACs towards electrochemical CO_2 RR are closely related to the M–N_x ($x = 1$–4) or M–C coordination environments, and the surrounding defects. In addition, according to the previous reports, the morphology and surface properties of supports are also important factors for the CO_2 adsorption capability and the catalytic performances of SACs.

3. Optimization strategies

The electronic structure of metal atoms is closely related to the adsorption of CO_2, the formation of intermediates and the desorption of products of CO_2 RR. Regulating the local

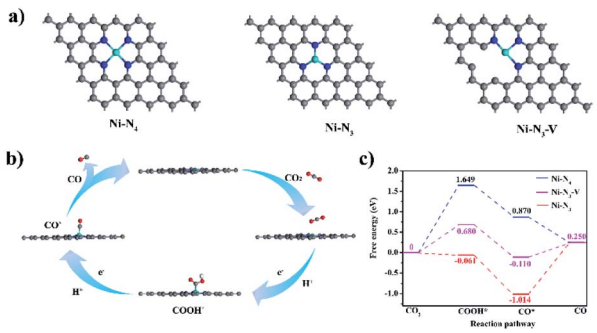

Fig. 12 (a) The optimized structures for Ni–N_4, Ni–N_3 and Ni–N_3–V. (b) Proposed reaction pathways of Ni–N_3–V for CO_2 RR. (c) The calculated free energy diagram for CO_2-to-CO conversion. Ref. 51 Copyright 2019, Wiley-VCH.

environment of metal sites is regarded as an efficient way to optimize the electronic structure of metal sites of SACs, and to improve the performances for electrochemical CO_2 RR.[45,60] In this section, we will highlight the optimization strategies in the following aspects, including reducing the coordination number, tuning the coordination atoms, engineering the axial chemical environment and constructing defects in supports.

3.1 Reducing the number of coordinated nitrogen atoms

According to the literature,[45,77] the decrease of the numbers of coordinated nitrogen atoms could efficiently optimize the performance of SACs for CO_2 RR. As shown in Fig. 13a, the coordination numbers of Co atoms in Co SACs could be regulated by tuning the pyrolysis temperature.[45] With the temperature elevating, more Co^{II}–imidazolate–Co^{II} linkages would decompose, leading to impaired Co–N bonds, and thus SACs with Co–N_4, Co–N_3 and Co–N_2 sites could be obtained. As shown in Fig. 13b, the XRD of Co SACs was performed, showing that no Co NPs were formed. The authors further investigated the coordination structures and crystal structures of Co–N_4, Co–N_3 and Co–N_2. The EXFAS spectra (Fig. 13c) show that the peak intensity corresponding to Co–N decreases as the coordination number decreases. Besides, from the XANES (Fig. 13d) and XPS (Fig. 13e) it can be seen that the oxidation state of Co is between 0 and +2, and also

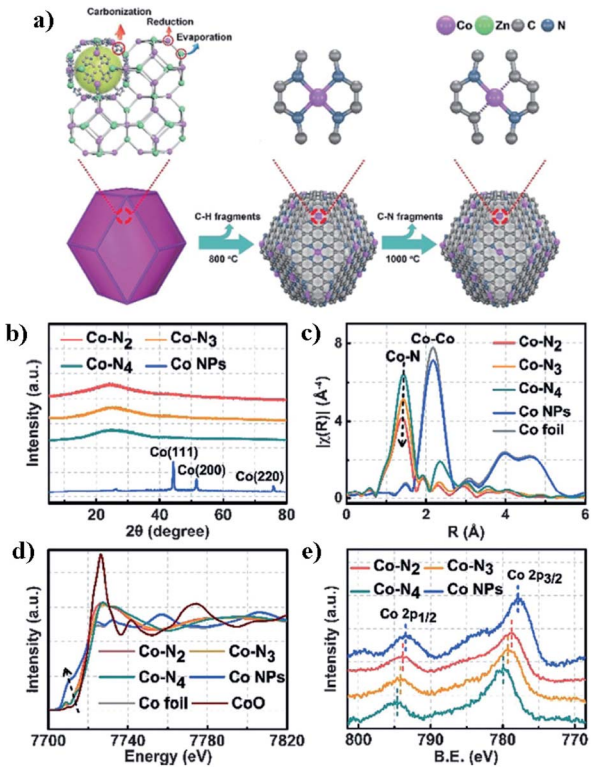

Fig. 13 (a) The schematic illustration of the synthesis of Co–N_4 and Co–N_2. (b) The XRD patterns for Co SACs and Co nanoparticles. (c and d) The EXAFS (c), the XANES (d) and XPS (d) spectra for Co SACs and comparison samples. Ref. 45 Copyright 2018, Wiley-VCH.

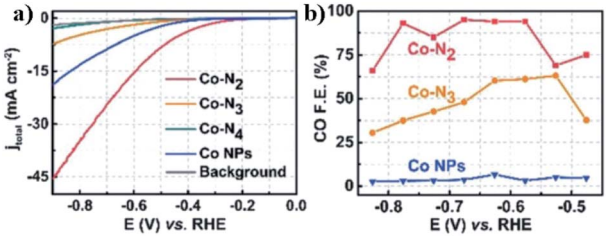

Fig. 14 (a) The linear sweep voltammetry for different catalysts. (b) The FE of CO for Co SACs with Co–N_4, Co–N_3 and Co–N_2 coordination environments. Ref. 45 Copyright 2018, Wiley-VCH.

decreases as the coordination number decreases. By DFT calculation, it is discovered that decreasing the coordination numbers of Co site results in an upward-shifted d-band center of Co, and thus the stronger *CO_2* bonding. Therefore, the current density and FE of CO were substantially enhanced (Fig. 14a and b).

Recently, Gong *et al.* prepared three types of Ni SACs by introducing polypyrrole into MgNi-MOF-74 and changing the pyrolysis temperature, to generate a series of NiSA–N_x–C ($x = 4$, 3 or 2).[77] As shown in Fig. 15a, the XANES spectra exhibit that the Ni valence in NiSA–N_x–C was between Ni^0 and Ni^{2+}. In addition, the FT-EXAFS spectra (Fig. 15b) show that the Ni–N (~1.36 Å) and Ni–C (~1.87 Å) peaks were observed in all Ni_{SA}–N_x–C samples and no obvious Ni–Ni bond was found. The fitting results confirm that the Ni–N coordination numbers are 4.0, 3.4 and 2.0 for Ni_{SA}–N_4–C, Ni_{SA}–N_3–C and Ni_{SA}–N_2–C, respectively. DFT calculations showed that the free energy change for the rate-determining step (the formation of COOH*) for NiSA–N_2–C is lower than those of NiSA–N_4–C and NiSA–N_3–C. As a result, the NiSA–N_2–C catalyst showed the best performance for CO_2 electroreduction (Fig. 15c and d), with 98% FE of CO and a high turnover frequency of 1622 h^{-1}.

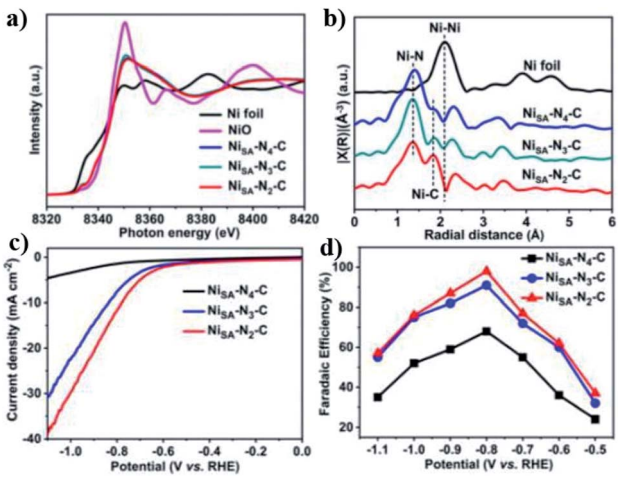

Fig. 15 (a) The Normalized Ni K-edge XANES spectra and (b) FE-EXAFS spectra for Ni_{SA}–N_x–C and comparison samples. (c) The linear sweep voltammetry and (d) The FE of CO for Ni_{SA}–N_x–C. The Ni Ref. 77 Copyright 2020, Wiley-VCH.

3.2 Tuning the coordination atoms

Besides the coordination number, the coordination atoms around the metal sites in SACs also play a key role in regulating the performances for CO_2 RR.[61,77] For example, Yang *et al.* reported an A-Ni-NSG SAC by pyrolyzing melamine and nickel acetate together with L-cysteine.[61] The Ni atoms in A-Ni-NSG were coordinated to S and pyridinic N, which exhibits a weaker electronegativity than the pyrrolic N in Ni(II)Pc, resulting in Ni(I) centers with a d^9 electronic configuration. The low-valence Ni(I) sites proved to be efficient active sites for CO_2 RR to CO, giving a high specific current of 350 A $g_{catalyst}^{-1}$ with a turnover frequency of 14 800 h^{-1} and 97% FE for CO at a mild overpotential of 0.61 V.

Fan *et al.* prepared a Ni SAC with the Ni@N_3 (pyrrolic) site, which shows a CO FE exceeding 90% with a turnover frequency of 12 000 h^{-1} and metal mass activity of 10 600 mA mg^{-1}.[70] As shown in Fig. 16, the free energy changes for Ni@N_3 (pyridinic) and Ni (111) are highly endothermic, demonstrating that the Ni@N_3 (pyridinic) and Ni (111) could be poisoned by *CO easily and are not suitable to be catalysts for CO_2 RR. However, the Ni@N_3 (pyrrolic) exhibits a free energy change of −0.03 eV, showing the easy desorption of CO. In addition, the free energy change for COOH* is more negative than that of H* on Ni@N_3 (pyrrolic), indicating that the process for CO_2-to-CO conversion is thermodynamically more favourable than the hydrogen evolution reaction. This work discovers the important role of coordinated nitrogen in Ni SACs and shows that Ni@N_3 (pyrrolic) sites could be the more suitable sites for CO_2 RR than Ni@N_3 (pyridinic).

In addition, introducing another metal atom to form isolated diatomic metal sites has also been proved to be a powerful strategy to alter the catalytic process by reducing the energy barriers during CO_2 RR. For example, Ren *et al.* reported a Ni/Fe–N–C catalyst, which featured isolated diatomic Ni–Fe sites (shown in the inset of Fig. 17a).[78] As shown in Fig. 17a, Ni/Fe–N–C shows much better performances for CO_2-to-CO conversion, with a current density higher than those of Ni–N–C and Fe–N–C. The results of DFT calculations (Fig. 17b) indicate that the rate-determining steps of CO_2 RR on Ni–N–C and Fe–N–C are the formation of COOH* and the desorption of CO, respectively. After the formation of the diatomic Ni/Fe–N–C SAC, it first undergoes a reduction of CO_2 to CO to generate a CO bridged species of Ni(CO)Fe–N–C (Fig. 17c(ii)), which will decrease the energy barriers for the formation of COOH* and the desorption of CO on Ni(CO)Fe–N–C (Fig. 17b and c(ii–iv)), resulting in a higher electrocatalytic activity of the diatomic Ni–Fe SAC for CO_2 electroreduction.

3.3 Engineering the axial chemical environment

The axial coordination environment of metal sites in SACs can be engineered by the axial interactions between metal atoms and supports, which is one of the important factors to immobilize the metal atoms and alter their electronic structures.[42,67,79–81] Han *et al.* found that the ultrathin nanosheets of STPyP-Co, which was obtained through the intermolecular assembly of tetra(4-pyridyl) porphyrin cobalt(II) (MTPyP-Co) monomers (Fig. 18a) between the axial coordination of Co(II) in one MTPyP-Co and the pyridine N in adjacent MTPyP-Co molecules, showed a much higher electrocatalytic activity for CO_2-to-CO conversion than MTPyP-Co.[79] They found that the axial coordination between the pyridine N and Co site in STPyP-Co (Fig. 18a) significantly elevates the energy level of the Co dz^2 orbital (Fig. 18b), resulting in the much lower energy barrier for the formation of COOH* (Fig. 18c), and thus the superior catalytic activity for CO_2 RR.

Wang *et al.* tuned the axial coordination of Co sites by introducing different heteroatoms into the graphene support, and constructed three types of Co SACs.[80] The graphitic sulfoxide dopants in graphene could be more efficient sites than –COOH groups to bind with Co atoms in NapCo through the formation of the Co–O bond, because of the enhanced electron communication in the as-prepared NapCo@SNG, which exhibited a three-fold increased turnover frequency for CO

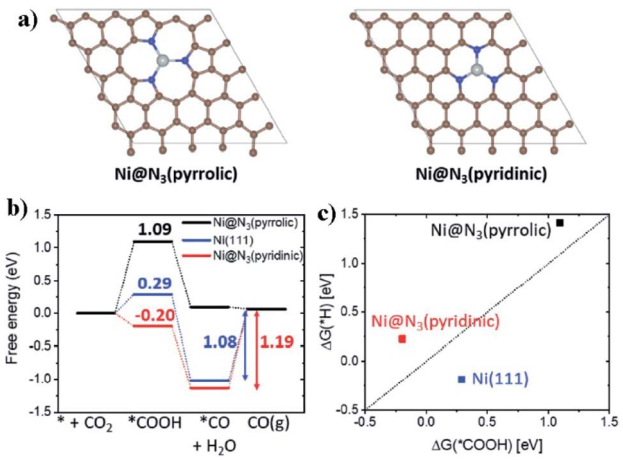

Fig. 16 (a) The calculation models of Ni@N_3 (pyrrolic) and Ni@N_3 (pyridinic). (b) Free energy diagram of electrocatalytic CO_2-to-CO. (c) Comparison of ΔG(*H) and ΔG(*COOH). Ref. 70 Copyright 2019, Wiley-VCH.

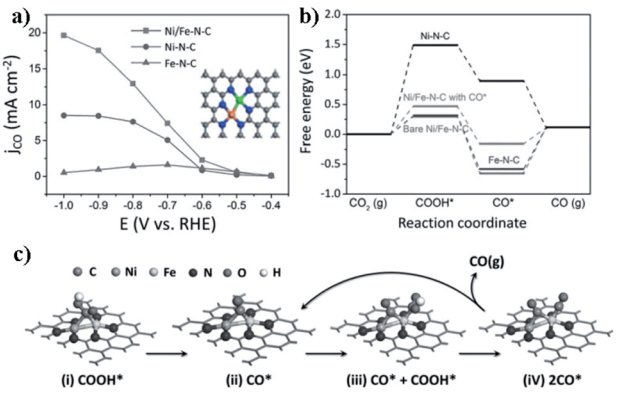

Fig. 17 (a) The partial current densities for the CO production of Ni/Fe–N–C, Ni–N–C and Fe–N–C SACs. The inset is the structural model for Ni/Fe–N–C. (b) The calculated free energy diagrams for CO_2-to-CO conversion on different catalysts. (c) The catalytic mechanism on Ni/Fe–N–C with the optimized structures for adsorbed intermediates of COOH* and CO*. Ref. 78 Copyright 2019, Wiley-VCH.

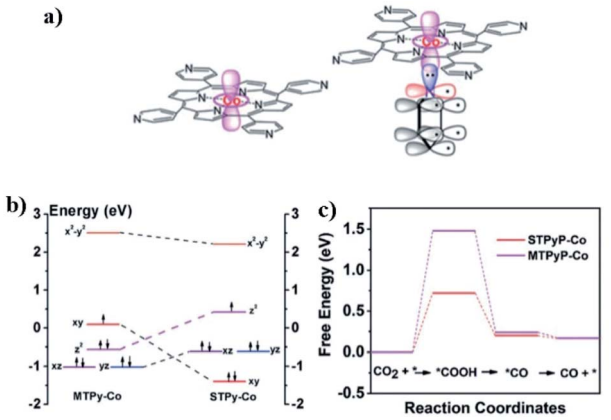

Fig. 18 (a) The structure of MTPyP-Co (left), and the interaction between the pyridine N and Co site in STPyP-Co (right). (b) The Co 3d orbital splitting in MTPyP-Co and STPyP-Co. (c) The calculated free energy diagram for CO_2 RR to CO on STPyPCo and MTPyP-Co. Ref. 79 Copyright 2019, Wiley-VCH.

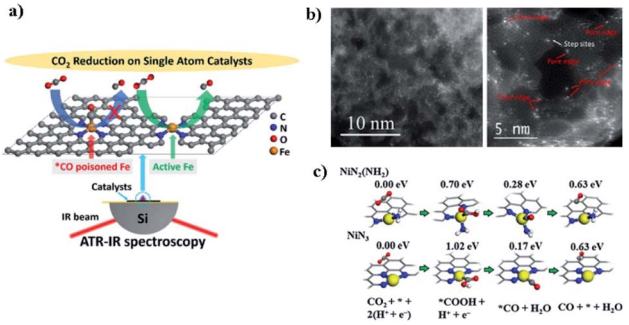

Fig. 19 (a) The real active sites on a heterogeneous Fe SAC in electrochemical CO_2 RR. Ref. 82 Copyright 2019, American Chemical Society. (b) The aberration-corrected scanning TEM images for Ni–N-MEGO. (c) The reaction pathway and corresponding free energy on the edge-anchored NiN_3 and $NiN_2(NH_2)$. Ref. 83 Copyright 2019, Elsevier.

production. The advantage of axial coordination for improving the CO_2-to-CO conversion was also found in Co–N_5,[42] which was prepared by anchoring CoPc on N-doped carbon supports through the Co–pyrrolic N bond; similar results were also found in Fe–N_5 sites supported on N-doped graphene with axial pyrrolic-N ligand coordinated with FeN_4.[67]

In addition, engineering the axial chemical environment could also improve the performance of active sites on the supports for CO_2 RR. For example, Lin *et al.* anchored CoPc on Fe–N–C supports (CoPc@Fe–N–C), which showed much better catalytic performances than CoPc, Fe–N–C and other comparison samples.[81] The DFT calculation shows that the anchored CoPc benefits the CO desorption and restrains the HER over Fe sites on the supports, leading to a markedly enhanced catalytic ability for CO_2-to-CO conversion.

3.4 Constructing defects in supports

Introducing more defects around the metal atoms or porosity in supports is also an effective way to improve the activity of SACs through strengthening the adsorption of CO_2.[51,62,82–85] For example, a controllable synthesis route of Ni SACs with vacancy defects around Ni–N_3 sites was developed (see the Synthesis section).[51] The experimental and calculation results show that the vacancy defects play a crucial role in improving the activity of Ni–N_3 sites, demonstrating the advantages of defect engineering for optimizing the electrocatalytic performances of SACs.

Recently, Qin *et al.* studied the real active sites in an Fe SAC for CO_2 RR by *in situ* infrared absorption spectroscopy and theoretical calculations.[82] As shown in Fig. 19a, the CO_2-to-CO conversion mainly proceeds on the Fe–N_4 sites embedded in a defective carbon layer. By contrast, the Fe centers of Fe–N_4 anchored on the complete graphitic layer can be easily poisoned by CO owing to the strong CO adsorption. The results inspired the researchers to pay more attention to the local environment of the metal centers in SACs. In addition, because the porosity in the support of SACs could affect the mass transfer and kinetics of CO_2 RR, and may also lead to more effective metal sites at the porous edge of the supports, it is of great value to design porous SACs. For example, Cheng *et al.* designed an unsaturated edge-anchored Ni SAC on porous graphene oxide (denoted as Ni–N-MEGO, with a high Ni loading of ~6.9 wt%), and assessed its performance for CO_2 RR.[83] As shown in Fig. 19b, the atomic Ni sites were mainly anchored on the edges of nanopores and acted as the essential active sites. The DFT calculation suggests that the edge-anchored Ni atoms with unsaturated nitrogen coordination environment show much higher performances for CO_2 electroreduction than those of in-plane structures (Fig. 19c).

Recently, Hu *et al.* prepared Fe SACs on N-doped carbon supports by a ZIF-assisted strategy with or without SiO_2 coating, and obtained Fe-CNPs and Fe-CNPs-w/o, respectively.[85] As

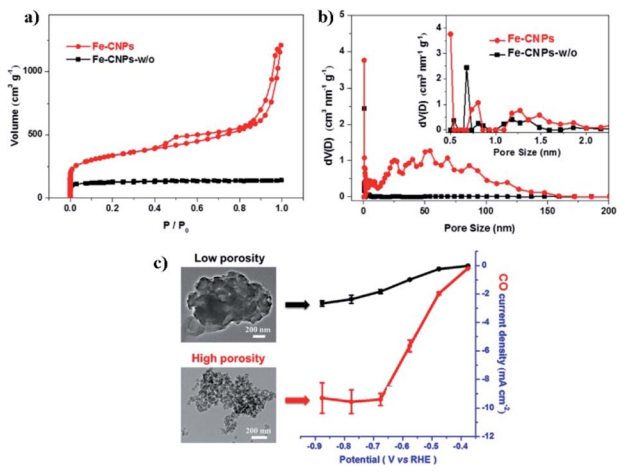

Fig. 20 (a) N_2 adsorption–desorption isotherms of Fe-CNPs and Fe-CNPs-w/o. (b) Pore size distribution curves of Fe-CNPs and Fe-CNPs-w/o. The inset is the magnification of the microporous span. (c) Porosity-induced high activity for CO_2 electroreduction to CO on Fe-CNPs (low porosity) and Fe-CNPs-w/o (high porosity). On the left is the corresponding TEM images. Ref. 85 Copyright 2019, American Chemical Society.

shown in Fig. 20a and b, Fe-CNPs showed a high specific area (1156.6 $m^2 g^{-1}$) and a total pore volume (0.49 $cm^3 g^{-1}$) with the pore diameters mainly of 0.8, 1.2 and 52 nm. By contrast, for Fe-CNPs-w/o, the specific area (360.1 $m^2 g^{-1}$) is quite low, and pore diameters were only 0.7 and 1.2 nm. As a result, compared with Fe-CNPs-w/o, Fe-CNPs showed better performances for CO_2-to-CO conversion with a higher FE (98.8%) and current density (Fig. 20c). This work highlights the porosity-dependent activity and selectivity for CO_2 electroreduction in SACs.

4. Conclusions and outlook

As a new class of heterogeneous catalysts, SACs feature highly exposed active sites with maximized atom utilization efficiency, and unique electronic and geometric structures, which all contribute to their high performances for electrochemical CO_2 RR. The tunable coordination environment of metal sites and support structures in SACs facilitate the optimization of their catalytic performances. In this review, newly developed synthesis methods and optimization strategies have been summarized and discussed. Although SACs hold great promise for high-efficiency conversion of CO_2 *via* the electroreduction process, there remain many problems that are yet to be addressed. For the development of SACs for CO_2 RR, the preparation needs to focus on the following aspects: (1) to controllably construct the local environment of metal sites and the porosity in supports; (2) to elevate the loading amounts of metal atoms with high activity while avoiding their agglomeration; (3) to improve the selectivity for a single, specific CO_2 reduction product and enhancing the stability; (4) to fabricate self-supporting electrodes to circumvent the use of polymer binders; (5) to develop universal preparation strategies; (6) to realize large-scale preparation with low cost for practical applications. In addition, for the related SACs developed thus far, the primary reduction product is CO, which is known to have been widely used for industrial production of chemicals such as methanol, acetic acid and hydrocarbons.[86] CO is also the key intermediate during the synthesis of multi-carbon (C_{2+}) products *via* electrochemical CO_2 RR.[87] Therefore, further integrating the already developed SACs with other electrocatalysts (typically, Cu-based catalysts) may achieve tandem catalysis from CO_2 to C_{2+}.[88]

In addition, more effort should be devoted to investigating the underlying mechanisms of the catalytic process on SACs. And the prerequisite for precise identification of the active sites at the atomic scale is to prepare SACs with well-defined metal coordination environments and controllable structures. On the basis of the successful fabrication of SACs with clear structures, and the combination of DFT calculations and more *in situ* characterization techniques available, the study of the nature of active sites in SACs could go more deeply.

Tuning the local environments of metal sites, including altering their coordination environments and constructing defects in supports, has been verified as an effective strategy for improving the activity and selectivity of SACs for CO_2 RR. The further advance in synthesis methodology and mechanism study for SACs would lead to more efficient optimization of the electrocatalytic performances of CO_2 RR. Given the great advantages of SACs, we believe more progress will be achieved in the area of CO_2 electroreduction.

Conflicts of interest

There are no conflicts to declare.

Acknowledgements

This work was supported by the National Key R&D Program of China (2017YFA0700104), the National Natural Science Foundation of China (21931007 and 21805207), 111 Project of China (D17003), and the Science & Technology Development Fund of Tianjin Education Commission for Higher Education (2018KJ129).

Notes and references

1 S. Chu, Y. Cui and N. Liu, *Nat. Mater.*, 2017, **16**, 16.
2 H. Rao, L. C. Schmidt, J. Bonin and M. Robert, *Nature*, 2017, **548**, 74.
3 L. Wang, W. Chen, D. Zhang, Y. Du, R. Amal, S. Qiao, J. Wu and Z. Yin, *Chem. Soc. Rev.*, 2019, **48**, 5310.
4 T. Liu, S. Ali, Z. Lian, B. Li and D. S. Su, *J. Mater. Chem. A*, 2017, **5**, 21596.
5 T. Ouyang, H.-J. Wang, H.-H. Huang, J.-W. Wang, S. Guo, W.-J. Liu, D.-C. Zhong and T.-B. Lu, *Angew. Chem., Int. Ed.*, 2018, **57**, 16480.
6 S. Tang, X. Yin, G. Wang, X. Lu and T. Lu, *Nano Res.*, 2019, **12**, 457.
7 L. Zhang, Z.-J. Zhao, T. Wang and J. Gong, *Chem. Soc. Rev.*, 2018, **47**, 5423.
8 S. Lin, C. S. Diercks, Y.-B. Zhang, N. Kornienko, E. M. Nichols, Y. Zhao, A. R. Paris, D. Kim, P. Yang, O. M. Yaghi and C. J. Chang, *Science*, 2015, **349**, 1208.
9 S. Gao, Y. Lin, X. Jiao, Y. Sun, Q. Luo, W. Zhang, D. Li, J. Yang and Y. Xie, *Nature*, 2016, **529**, 68.
10 S. Ren, D. Joulié, D. Salvatore, K. Torbensen, M. Wang, M. Robert and C. P. Berlinguette, *Science*, 2019, **365**, 367.
11 J. Jiao, R. Lin, S. Liu, W.-C. Cheong, C. Zhang, Z. Chen, Y. Pan, J. Tang, K. Wu, S.-F. Hung, H. M. Chen, L. Zheng, Q. Lu, X. Yang, B. Xu, H. Xiao, J. Li, D. Wang, Q. Peng, C. Chen and Y. Li, *Nat. Chem.*, 2019, **11**, 222.
12 M. Schreier, F. Héroguel, L. Steier, S. Ahmad, J. S. Luterbacher, M. T. Mayer, J. Luo and M. Grätzel, *Nat. Energy*, 2017, **2**, 17087.
13 B. Khezri, A. C. Fisher and M. Pumera, *J. Mater. Chem. A*, 2017, **5**, 8230.
14 D. D. Zhu, J. L. Liu and S. Z. Qiao, *Adv. Mater.*, 2016, **28**, 3423.
15 Z. Sun, T. Ma, H. Tao, Q. Fan and B. Han, *Chem*, 2017, **3**, 560.
16 Y. Wang, J. Liu, Y. Wang, A. M. Al-Enizi and G. Zheng, *Small*, 2017, **13**, 1701809.
17 (*a*) W. Zhu, R. Michalsky, Ö. Metin, H. Lv, S. Guo, C. J. Wright, X. Sun, A. A. Peterson and S. Sun, *J. Am. Chem. Soc.*, 2013, **135**, 16833; (*b*) X. Ma, Y. Shen, S. Yao, C. An, W. Zhang, J. Zhu, R. Si, C. Guo and C. An, *J. Mater. Chem. A*, 2020, **8**, 3344; (*c*) J. H. Lee, S. Kattel, Z. Xie,

B. M. Tackett, J. Wang, C.-J. Liu and J. G. Chen, *Adv. Funct. Mater.*, 2018, **28**, 1804762.
18 X. Feng, K. Jiang, S. Fan and M. W. Kanan, *J. Am. Chem. Soc.*, 2015, **137**, 4606.
19 N. Han, Y. Wang, H. Yang, J. Deng, J. Wu, Y. Li and Y. Li, *Nat. Commun.*, 2018, **9**, 1320.
20 L. Lu, X. Sun, J. Ma, D. Yang, H. Wu, B. Zhang, J. Zhang and B. Han, *Angew. Chem., Int. Ed.*, 2018, **57**, 14149.
21 S. Liu, J. Xiao, X. F. Lu, J. Wang, X. Wang and X. W. Lou, *Angew. Chem., Int. Ed.*, 2019, **58**, 8499.
22 S. Liu, X. F. Lu, J. Xiao, X. Wang and X. W. Lou, *Angew. Chem., Int. Ed.*, 2019, **58**, 13828.
23 Y. He, W.-J. Jiang, Y. Zhang, L.-B. Huang and J.-S. Hu, *J. Mater. Chem. A*, 2019, **7**, 18428.
24 S. Liu, H. Tao, Q. Liu, Z. Xu, Q. Liu and J.-L. Luo, *ACS Catal.*, 2018, **8**, 1469.
25 Z. Zhao, X. Peng, X. Liu, X. Sun, J. Shi, L. Han, G. Li and J. Luo, *J. Mater. Chem. A*, 2017, **5**, 20239.
26 A. T. Landers, M. Fields, D. A. Torelli, J. Xiao, T. R. Hellstern, S. A. Francis, C. Tsai, J. Kibsgaard, N. S. Lewis, K. Chan, C. Hahn and T. F. Jaramillo, *ACS Energy Lett.*, 2018, **3**, 1450.
27 X. Sun, L. Lu, Q. Zhu, C. Wu, D. Yang, C. Chen and B. Han, *Angew. Chem., Int. Ed.*, 2018, **57**, 2427.
28 (*a*) F. Lei, W. Liu, Y. Sun, J. Xu, K. Liu, L. Liang, T. Yao, B. Pan, S. Wei and Y. Xie, *Nat. Commun.*, 2016, **7**, 12697; (*b*) X. Zheng, P. De Luna, F. P. García de Arquer, B. Zhang, N. Becknell, M. B. Ross, Y. Li, M. N. Banis, Y. Li, M. Liu, O. Voznyy, C. T. Dinh, T. Zhuang, P. Stadler, Y. Cui, X. Du, P. Yang and E. H. Sargent, *Joule*, 2017, **1**, 794; (*c*) S. Zhao, S. Li, T. Guo, S. Zhang, J. Wang, Y. Wu and Y. Chen, *Nano-Micro Lett.*, 2019, **11**, 62.
29 (*a*) K. Fan, Y. Jia, Y. Ji, P. Kuang, B. Zhu, X. Liu and J. Yu, *ACS Catal.*, 2020, **10**, 358; (*b*) J.-H. Zhou, K. Yuan, L. Zhou, Y. Guo, M.-Y. Luo, X.-Y. Guo, Q.-Y. Meng and Y.-W. Zhang, *Angew. Chem., Int. Ed.*, 2019, **58**, 14197; (*c*) X. Zhang, X. Sun, S.-X. Guo, A. M. Bond and J. Zhang, *Energy Environ. Sci.*, 2019, **12**, 1334.
30 (*a*) D. Bohra, I. Ledezma-Yanez, G. Li, W. de Jong, E. A. Pidko and W. A. Smith, *Angew. Chem., Int. Ed.*, 2019, **58**, 1345; (*b*) S. Liu, C. Sun, J. Xiao and J.-L. Luo, *ACS Catal.*, 2020, **10**, 3158; (*c*) D. Sun, X. Xu, Y. Qin, S. P. Jiang and Z. Shao, *ChemSusChem*, 2020, **13**, 39.
31 H. Mistry, R. Reske, Z. Zeng, Z.-J. Zhao, J. Greeley, P. Strasser and B. R. Cuenya, *J. Am. Chem. Soc.*, 2014, **136**, 16473.
32 D. Gao, H. Zhou, J. Wang, S. Miao, F. Yang, G. Wang, J. Wang and X. Bao, *J. Am. Chem. Soc.*, 2015, **137**, 4288.
33 R. Reske, H. Mistry, F. Behafarid, B. Roldan Cuenya and P. Strasser, *J. Am. Chem. Soc.*, 2014, **136**, 6978.
34 (*a*) X.-F. Yang, A. Wang, B. Qiao, J. Li, J. Liu and T. Zhang, *Acc. Chem. Res.*, 2013, **46**, 1740; (*b*) A. Wang, J. Li and T. Zhang, *Nat. Rev. Chem.*, 2018, **2**, 65.
35 B. Qiao, A. Wang, X. Yang, L. F. Allard, Z. Jiang, Y. Cui, J. Liu, J. Li and T. Zhang, *Nat. Chem.*, 2011, **3**, 634.
36 X.-P. Yin, H.-J. Wang, S.-F. Tang, X.-L. Lu, M. Shu, R. Si and T.-B. Lu, *Angew. Chem., Int. Ed.*, 2018, **57**, 9382.
37 N. Zhang, T. Zhou, M. Chen, H. Feng, R. Yuan, C. a. Zhong, W. Yan, Y. Tian, X. Wu, W. Chu, C. Wu and Y. Xie, *Energy Environ. Sci.*, 2020, **13**, 111.
38 (*a*) Y. Wang, Z. Chen, P. Han, Y. Du, Z. Gu, X. Xu and G. Zheng, *ACS Catal.*, 2018, **8**, 7113; (*b*) M.-J. Cheng, E. L. Clark, H. H. Pham, A. T. Bell and M. Head-Gordon, *ACS Catal.*, 2016, **6**, 7769.
39 Y. Cheng, S. Yang, S. P. Jiang and S. Wang, *Small Methods*, 2019, **3**, 1800440.
40 Y. Chen, S. Ji, C. Chen, Q. Peng, D. Wang and Y. Li, *Joule*, 2018, **2**, 1242.
41 S. Ding, M. J. Hülsey, J. Pérez-Ramírez and N. Yan, *Joule*, 2019, **3**, 2897.
42 Y. Pan, R. Lin, Y. Chen, S. Liu, W. Zhu, X. Cao, W. Chen, K. Wu, W.-C. Cheong, Y. Wang, L. Zheng, J. Luo, Y. Lin, Y. Liu, C. Liu, J. Li, Q. Lu, X. Chen, D. Wang, Q. Peng, C. Chen and Y. Li, *J. Am. Chem. Soc.*, 2018, **140**, 4218.
43 J. Gu, C.-S. Hsu, L. Bai, H. M. Chen and X. Hu, *Science*, 2019, **364**, 1091.
44 J. Guo, J. Huo, Y. Liu, W. Wu, Y. Wang, M. Wu, H. Liu and G. Wang, *Small Methods*, 2019, **3**, 1900159.
45 X. Wang, Z. Chen, X. Zhao, T. Yao, W. Chen, R. You, C. Zhao, G. Wu, J. Wang, W. Huang, J. Yang, X. Hong, S. Wei, Y. Wu and Y. Li, *Angew. Chem., Int. Ed.*, 2018, **57**, 1944.
46 C. Zhao, X. Dai, T. Yao, W. Chen, X. Wang, J. Wang, J. Yang, S. Wei, Y. Wu and Y. Li, *J. Am. Chem. Soc.*, 2017, **139**, 8078.
47 H. Yang, Y. Wu, G. Li, Q. Lin, Q. Hu, Q. Zhang, J. Liu and C. He, *J. Am. Chem. Soc.*, 2019, **141**, 12717.
48 W. Bi, X. Li, R. You, M. Chen, R. Yuan, W. Huang, X. Wu, W. Chu, C. Wu and Y. Xie, *Adv. Mater.*, 2018, **30**, 1706617.
49 C. Zhao, Y. Wang, Z. Li, W. Chen, Q. Xu, D. He, D. Xi, Q. Zhang, T. Yuan, Y. Qu, J. Yang, F. Zhou, Z. Yang, X. Wang, J. Wang, J. Luo, Y. Li, H. Duan, Y. Wu and Y. Li, *Joule*, 2019, **3**, 584.
50 J. Yang, Z. Qiu, C. Zhao, W. Wei, W. Chen, Z. Li, Y. Qu, J. Dong, J. Luo, Z. Li and Y. Wu, *Angew. Chem., Int. Ed.*, 2018, **57**, 14095.
51 X. Rong, H.-J. Wang, X.-L. Lu, R. Si and T.-B. Lu, *Angew. Chem., Int. Ed.*, 2020, **59**, 1961.
52 M. Wang, L. Árnadóttir, Z. J. Xu and Z. Feng, *Nano-Micro Lett.*, 2019, **11**, 47.
53 X. Li, W. Bi, M. Chen, Y. Sun, H. Ju, W. Yan, J. Zhu, X. Wu, W. Chu, C. Wu and Y. Xie, *J. Am. Chem. Soc.*, 2017, **139**, 14889.
54 Y. Cheng, S. Zhao, B. Johannessen, J.-P. Veder, M. Saunders, M. R. Rowles, M. Cheng, C. Liu, M. F. Chisholm, R. De Marco, H.-M. Cheng, S.-Z. Yang and S. P. Jiang, *Adv. Mater.*, 2018, **30**, 1706287.
55 H. Yang, L. Shang, Q. Zhang, R. Shi, G. I. N. Waterhouse, L. Gu and T. Zhang, *Nat. Commun.*, 2019, **10**, 4585.
56 T. Zheng, K. Jiang, N. Ta, Y. Hu, J. Zeng, J. Liu and H. Wang, *Joule*, 2019, **3**, 265.
57 F. Pan, W. Deng, C. Justiniano and Y. Li, *Appl. Catal., B*, 2018, **226**, 463.
58 C. Zhang, S. Yang, J. Wu, M. Liu, S. Yazdi, M. Ren, J. Sha, J. Zhong, K. Nie, A. S. Jalilov, Z. Li, H. Li, B. I. Yakobson,

Q. Wu, E. Ringe, H. Xu, P. M. Ajayan and J. M. Tour, *Adv. Energy Mater.*, 2018, **8**, 1703487.
59 F. Pan, H. Zhang, K. Liu, D. Cullen, K. More, M. Wang, Z. Feng, G. Wang, G. Wu and Y. Li, *ACS Catal.*, 2018, **8**, 3116.
60 Z. Geng, Y. Cao, W. Chen, X. Kong, Y. Liu, T. Yao and Y. Lin, *Appl. Catal., B*, 2019, **240**, 234.
61 H. B. Yang, S.-F. Hung, S. Liu, K. Yuan, S. Miao, L. Zhang, X. Huang, H.-Y. Wang, W. Cai, R. Chen, J. Gao, X. Yang, W. Chen, Y. Huang, H. M. Chen, C. M. Li, T. Zhang and B. Liu, *Nat. Energy*, 2018, **3**, 140.
62 C. Yan, H. Li, Y. Ye, H. Wu, F. Cai, R. Si, J. Xiao, S. Miao, S. Xie, F. Yang, Y. Li, G. Wang and X. Bao, *Energy Environ. Sci.*, 2018, **11**, 1204.
63 P. Su, K. Iwase, S. Nakanishi, K. Hashimoto and K. Kamiya, *Small*, 2016, **12**, 6083.
64 F. Yang, P. Song, X. Liu, B. Mei, W. Xing, Z. Jiang, L. Gu and W. Xu, *Angew. Chem., Int. Ed.*, 2018, **57**, 12303.
65 E. Zhang, T. Wang, K. Yu, J. Liu, W. Chen, A. Li, H. Rong, R. Lin, S. Ji, X. Zheng, Y. Wang, L. Zheng, C. Chen, D. Wang, J. Zhang and Y. Li, *J. Am. Chem. Soc.*, 2019, **141**, 16569.
66 Y. Zhao, J. Liang, C. Wang, J. Ma and G. G. Wallace, *Adv. Energy Mater.*, 2018, **8**, 1702524.
67 H. Zhang, J. Li, S. Xi, Y. Du, X. Hai, J. Wang, H. Xu, G. Wu, J. Zhang, J. Lu and J. Wang, *Angew. Chem., Int. Ed.*, 2019, **58**, 14871.
68 H. Yang, Q. Lin, C. Zhang, X. Yu, Z. Cheng, G. Li, Q. Hu, X. Ren, Q. Zhang and J. Liu, *Nat. Commun.*, 2020, **11**, 1.
69 S. Gao, Z. Sun, W. Liu, X. Jiao, X. Zu, Q. Hu, Y. Sun, T. Yao, W. Zhang, S. Wei and Y. Xie, *Nat. Commun.*, 2017, **8**, 14503.
70 Q. Fan, P. Hou, C. Choi, T.-S. Wu, S. Hong, F. Li, Y.-L. Soo, P. Kang, Y. Jung and Z. Sun, *Adv. Energy Mater.*, 2020, **10**, 1903068.
71 Z. Zhang, J. Xiao, X.-J. Chen, S. Yu, L. Yu, R. Si, Y. Wang, S. Wang, X. Meng, Y. Wang, Z.-Q. Tian and D. Deng, *Angew. Chem., Int. Ed.*, 2018, **57**, 16339.
72 J. Li, P. Pršlja, T. Shinagawa, A. J. Martín Fernández, F. Krumeich, K. Artyushkova, P. Atanassov, A. Zitolo, Y. Zhou, R. García-Muelas, N. López, J. Pérez-Ramírez and F. Jaouen, *ACS Catal.*, 2019, **9**, 10426.
73 J.-H. Liu, L.-M. Yang and E. Ganz, *J. Mater. Chem. A*, 2019, **7**, 3805.
74 S. Liu, H. B. Yang, S.-F. Hung, J. Ding, W. Cai, L. Liu, J. Gao, X. Li, X. Ren, Z. Kuang, Y. Huang, T. Zhang and B. Liu, *Angew. Chem., Int. Ed.*, 2020, **59**, 798.
75 W. Ju, A. Bagger, G.-P. Hao, A. S. Varela, I. Sinev, V. Bon, B. Roldan Cuenya, S. Kaskel, J. Rossmeisl and P. Strasser, *Nat. Commun.*, 2017, **8**, 944.
76 X. Zu, X. Li, W. Liu, Y. Sun, J. Xu, T. Yao, W. Yan, S. Gao, C. Wang, S. Wei and Y. Xie, *Adv. Mater.*, 2019, **31**, 1808135.
77 Y.-N. Gong, L. Jiao, Y. Qian, C.-Y. Pan, L. Zheng, X. Cai, B. Liu, S.-H. Yu and H.-L. Jiang, *Angew. Chem., Int. Ed.*, 2020, **59**, 2705.
78 W. Ren, X. Tan, W. Yang, C. Jia, S. Xu, K. Wang, S. C. Smith and C. Zhao, *Angew. Chem., Int. Ed.*, 2019, **58**, 6972.
79 J. Han, P. An, S. Liu, X. Zhang, D. Wang, Y. Yuan, J. Guo, X. Qiu, K. Hou, L. Shi, Y. Zhang, S. Zhao, C. Long and Z. Tang, *Angew. Chem., Int. Ed.*, 2019, **58**, 12711.
80 J. Wang, X. Huang, S. Xi, J.-M. Lee, C. Wang, Y. Du and X. Wang, *Angew. Chem., Int. Ed.*, 2019, **58**, 13532.
81 L. Lin, H. Li, C. Yan, H. Li, R. Si, M. Li, J. Xiao, G. Wang and X. Bao, *Adv. Mater.*, 2019, **31**, 1903470.
82 X. Qin, S. Zhu, F. Xiao, L. Zhang and M. Shao, *ACS Energy Lett.*, 2019, **4**, 1778.
83 Y. Cheng, S. Zhao, H. Li, S. He, J.-P. Veder, B. Johannessen, J. Xiao, S. Lu, J. Pan, M. F. Chisholm, S.-Z. Yang, C. Liu, J. G. Chen and S. P. Jiang, *Appl. Catal., B*, 2019, **243**, 294.
84 W. Zheng, J. Yang, H. Chen, Y. Hou, Q. Wang, M. Gu, F. He, Y. Xia, Z. Xia, Z. Li, B. Yang, L. Lei, C. Yuan, Q. He, M. Qiu and X. Feng, *Adv. Funct. Mater.*, 2019, 1907658.
85 C. Hu, S. Bai, L. Gao, S. Liang, J. Yang, S.-D. Cheng, S.-B. Mi and J. Qiu, *ACS Catal.*, 2019, **9**, 11579.
86 M. Jouny, G. S. Hutchings and F. Jiao, *Nat. Catal.*, 2019, **2**, 1062.
87 C. G. Morales-Guio, E. R. Cave, S. A. Nitopi, J. T. Feaster, L. Wang, K. P. Kuhl, A. Jackson, N. C. Johnson, D. N. Abram and T. Hatsukade, *Nat. Catal.*, 2018, **1**, 764.
88 M. Jouny, W. Luc and F. Jiao, *Nat. Catal.*, 2018, **1**, 748.

